Superlattice Hafnia-Zirconia-Alumina Nano-Electro-Mechanical Resonators for Integrated Super-High-Frequency Control

Troy Tharpe[1], Eitan Hershkovitz[2], Faysal Hakim[1], Honggyu Kim[2], Roozbeh Tabrizian[1*]

[1] *Department of Electrical and Computer Engineering,*

[2] *Department of Materials Science and Engineering,*

University of Florida, Gainesville, FL 32611, USA

Abstract

Multifunctional electronic systems rely indispensably on high quality-factor (Q) micro- and nano-electro-mechanical systems (M/NEMS) resonators for frequency control applications such as precise clock generation, synchronization, and radio-frequency wireless communication. Hundreds of high-performance M/NEMS resonators with frequencies extending over 32 kHz to 6 GHz are heterogeneously integrated with complementary metal oxide semiconductor (CMOS) circuits to form portable frequency control systems. However, heterogeneous integration imposes substantial overhead on critical system specifications, such as size and power consumption, as well as overall performance. This further limits system scalability for dynamic spectrum use and frequency extension to untapped bands in centimeter- and millimeter-wave regimes. Here, we present intrinsically switchable NEMS resonator building-blocks with ultra-wide-spectrum coverage for monolithic CMOS integration of frequency control systems, using superlattice hafnia-zirconia-alumina ($Hf_{0.5}Zr_{0.5}O_2$ – Al_2O_3) transducers. The superlattice structure along with ferroelastic re-orientation through pulsed poling enable large linear electromechanical coupling (k_t^2) and high-Q in $Hf_{0.5}Zr_{0.5}O_2$ – Al_2O_3 NEMS resonators, operating in lateral- and thickness-

*Corresponding Author. Email: rtabrizian@ece.ufl.edu

oriented bulk acoustic wave modes. Integrated NEMS resonators with frequencies (f) over 0.4 to 17.3 GHz, f-Q products up to 4.04×10^{12} and k_t^2s as high as 2.5%, are demonstrated by electrical measurements. Using DC bias voltage for depolarization of transducers, we show these resonators can be intrinsically switched off to their electromechanical noise floor, providing an on-off isolation as high as 37dB. Intrinsically switchable superlattice hafnia-zirconia-alumina NEMS resonators pave the way to realize switch-free, monolithic frequency control systems with multi-band operation towards mm-wave regime.

Main

Micro-electromechanical systems (MEMS) resonators serve as indispensable building blocks for frequency control applications in multifunctional electronic systems. MEMS resonators provide very large quality factors (Q) that are several orders of magnitude higher compared to their solid-state counterparts (*e.g.*, inductor-capacitor circuits)[1,2]. This enables creation of ultra-stable timing and frequency references that are essential for clock generation, synchronization, and navigation functionalities in modern electronic systems[3]. Further, piezoelectric MEMS resonators, also known as micro-acoustic passives, allow for the creation of highly selective, chip-scale, radiofrequency (RF) filters that facilitate spectral processing at the front-end of wireless communication modules[4,5].

Currently, hundreds of MEMS resonators are used in smart handheld wireless systems[6]. These resonators rely on only a few common operation mechanisms, such as electrostatic[7,8] and piezoelectric[9,10] electromechanical transduction, and use common constituent materials, including single crystal silicon (Si) and aluminum-nitride thin films[11,12]. Despite these commonalities, each

MEMS-based frequency control application requires a uniquely customized resonator fabrication process corresponding to a specific operation frequency. This imposes substantial manufacturing overhead that severely limits conventional MEMS technologies to provide standard resonator building-blocks with consistent performance across a wide spectrum and for diverse frequency control applications.

MEMS resonators customized for specific applications and operation frequencies are packaged in separate cases and integrated with interface control circuitry to create heterogenous frequency control systems. This non-monolithic integration sets two fundamental limits on the size, performance, and frequency scalability of systems. First, separate fabrication and packaging processes for resonators with different frequencies impose excessive size on the system that is not acceptable considering the emerging trend in modern wireless technologies that target the use of numerous bands over 0.1-100 GHz. Second, the non-monolithic integration of MEMS resonators and electronic circuits through two-dimensional routings induce excessive noise, interference and power consumption, all exacerbated by frequency scaling to centimeter- and millimeter-wave (cm- and mm-wave) regimes[6,13].

The ultimate solution to these fundamental limitations is monolithic integration of MEMS resonators on advanced semiconductor nodes. Since the advent of MEMS in 1965 with the resonant gate transistor[14], integration of high-Q electromechanical resonators at the front- or back-end-of-line (F/BEOL) of complementary metal-oxide-semiconductor (CMOS) chips has been investigated intermittently. However, now that modern wireless systems demand extreme frequency scaling, this goal has become imperative.

CMOS-monolithic MEMS resonators have been demonstrated through innovative design and integration approaches within fabrication limitations at FEOL and BEOL. The foremost example

of these efforts is the use of FinFET gate dielectrics along with acoustic energy localization, to realize high-Q MEMS resonators at FEOL[15,16]. Alternatively, demonstrations of BEOL-integrated MEMS resonators are reported using electrostatic or piezoelectric transducers integrated atop metal and insulating caping layers of CMOS[17,18]. These approaches generally rely on electrostatic transduction, which substantially limits the electromechanical coupling (k_t^2) of the resonator and makes extreme frequency scaling very challenging[19]. Further, approaches using piezoelectric films typically rely on materials that are not readily compatible with standard CMOS and do not provide thickness scalability into regimes that are comparable with solid-state components in advanced semiconductor nodes[20,21,22,23].

The discovery of ferroelectricity in hafnium dioxide (*i.e.*, hafnia) over a decade ago[24], along with the first demonstration of hafnia-zirconia ($Hf_xZr_{1-x}O_2$) as an nanoelectromechanical transducer[25], uniquely position $Hf_xZr_{1-x}O_2$ to solve the size, performance, and frequency scalability concerns of conventional MEMS resonators. By leveraging the inherent CMOS compatibility and outstanding scalability of atomic layer deposition (ALD), hafnia-zirconia ferroelectrics provide a transducer capable of monolithic integration within advanced CMOS nodes. Additionally, the transformative advantage of $Hf_xZr_{1-x}O_2$ over conventional perovskites and emerging nitride ferroelectrics is its ability to sustain a robust polarization even when scaled to 1nm thicknesses[26]. This scalability is pivotal in realization of high-performance piezoelectric nano electromechanical systems (NEMS). $Hf_xZr_{1-x}O_2$ transducers with thicknesses of just a few nanometers are poised to enable the creation of integrated, high-Q, NEMS resonators spanning super high frequency (SHF) and extremely high frequency (EHF) regimes[25,27,28].

In this article, we demonstrate hafnia-zirconia ($Hf_{0.5}Zr_{0.5}O_2$) NEMS resonators that provide consistently high Q and k_t^2 over the entire 0.39 to 17.32 GHz spectrum, through operating in lateral

and thickness-oriented bulk acoustic wave (BAW) modes. This high performance over multi-order of magnitude frequency design space is achieved via implementation of superlattice $Hf_{0.5}Zr_{0.5}O_2$ – Al_2O_3 transducers that sustain large piezoelectric coupling, despite relaxation of stress boundary conditions upon resonator release from its host substrate. Lateral operation allows for lithographically defined high-Q resonance modes, spanning 0.39 to 1.36 GHz, while thickness excitation allows for high-k_t^2 SHF resonance modes up to 17.32 GHz. The extracted frequency – Q product of up to 4.04×10^{12} and k_t^2 of 2.52% at SHF represent a substantial improvement over conventional NEMS counterparts at similar dimensions and frequencies [20,21,22]. Further, we demonstrate the intrinsic switchability of superlattice $Hf_{0.5}Zr_{0.5}O_2$ – Al_2O_3 NEMS resonators to electromechanical noise floor with 37dB on-off isolation, through ferroelectric depolarization of transducers. These attributes collectively highlight the promising potential of superlattice $Hf_{0.5}Zr_{0.5}O_2$ – Al_2O_3 NEMS resonators for creation of CMOS-monolithic reconfigurable frequency control systems for multi-band operation over SHF spectrum.

$Hf_{0.5}Zr_{0.5}O_2$ – Al_2O_3 Superlattice Transducer

Nanoscale $Hf_xZr_{1-x}O_2$ film deposited by CMOS-compatible ALD is inherently amorphous due to the low thermal budget during processing, which is insufficient for formation of crystalline domains. Rapid thermal annealing (RTA) can be used for crystallization of $Hf_xZr_{1-x}O_2$ film in one or multiple of its stable and meta-stable morphologies including orthorhombic (space group $Pca2_1$), tetragonal (space group $P4_2/nmc$), and monoclinic (space group $P2_1/c$) phases (see Supplementary Document, Section 1, for detailed discussion on crystalline structure of these morphologies). Among these, the orthorhombic phase is polar and therefore desirable for ferroelectric and piezoelectric device applications. However, due to the meta-stable nature of orthorhombic phase in $Hf_xZr_{1-x}O_2$, proper structural engineering is required for its promotion

during crystallization. The purpose of such structural engineering is formation of internal stress to stabilize polar orthorhombic phase and prevent its reversion to nonpolar counterparts. Various nanostructure engineering approaches have been developed for this purpose, including application of biaxial stress through the use of capping electrodes with highly different coefficient of thermal expansion (CTE)[29,30], limitation of grain sizes by periodic interruption of crystalline growth[31,32], introduction of dopants or oxygen vacancies during deposition[33,34], or application of electric field[35,36].

Extensive reports over the past decade highlight feasibility of CMOS-compatible growth of ferroelectric, orthorhombic $Hf_xZr_{1-x}O_2$ films over a wide range of thicknesses, from sub-1nm to 50nm[26,37]. When using $Hf_xZr_{1-x}O_2$ for creation of NEMS resonators over UHF and SHF regimes, opting for a thicker transducer enables enhancement of power-handling that is essential for implementation of low-noise oscillators and linear filters. However, scaling $Hf_xZr_{1-x}O_2$ thickness beyond 10nm results in a large stress gradient across the film, which translates to inefficient and nonuniform orthorhombic crystallization and consequently reduced polarization and piezoelectricity. Further, in free-standing $Hf_xZr_{1-x}O_2$ NEMS resonators, the stress relaxation that is geometrically imposed when releasing from host substrate, induces substantial conversion of orthorhombic domains to nonpolar monoclinic[38]. This post-release conversion, unique to $Hf_xZr_{1-x}O_2$ NEMS applications, is highly undesirable as it significantly reduces electromechanical coupling of the transducer.

In this work, efficient $Hf_xZr_{1-x}O_2$ transducers are created by formation of a superlattice that enables sustaining crystallization stress independent from geometrical relaxation (*i.e.*, cavity release) and thickness scaling. The superlattice transducer is created from alternate stacking of 9.2nm $Hf_{0.5}Zr_{0.5}O_2$ and 1nm alumina (Al_2O_3) layers. The complete transducer stack is comprised of 30

nm top and bottom $Hf_{0.5}Zr_{0.5}O_2$ layers, used for passivation during release, 20 nm top tungsten (W) electrode, 50 nm $Hf_{0.5}Zr_{0.5}O_2 – Al_2O_3$ superlattice, and 25 nm bottom W electrode. Stack schematic and high-resolution transmission electron microscopy (HR-TEM) images are displayed in Fig. 1 (a), while the 50 nm thick $Hf_{0.5}Zr_{0.5}O_2 – Al_2O_3$ superlattice transducer is highlighted by the HR-TEM image in Fig. 1 (b). Orthorhombic phase within superlattice transducers is evident by Fig. 1 (c) that shows a high-angle annular dark-field (HAADF) image recorded in scanning TEM (STEM), revealing the presence of a polar, orthorhombic grain projected along the [111] orthorhombic direction. Figure 1 (d) further illustrates a mapping of this [111] orthorhombic grain, showing a match of orthorhombic unit cell with a 15º rotation of the 2D projection for polar/c-axis, from surface normal.

$Hf_{0.5}Zr_{0.5}O_2 – Al_2O_3$ superlattice transducers provide several advantages for the realization of high-performance NEMS resonators. The mismatch in CTE of $Hf_{0.5}Zr_{0.5}O_2$ and Al_2O_3, along with the large elastic constant of Al_2O_3, induces a large tensile stress within the transducer, pivotal to sustaining orthorhombic phase even after cavity release. This concept is experimentally verified by comparing the evolution of diffraction peak patterns between pure $Hf_{0.5}Zr_{0.5}O_2$ and $Hf_{0.5}Zr_{0.5}O_2 – Al_2O_3$ superlattice over release. Figure 2 compares X-ray diffraction (XRD) patterns of 20nm monolayer $Hf_{0.5}Zr_{0.5}O_2$ (Fig. 2 (a)) and superlattice $Hf_{0.5}Zr_{0.5}O_2 – Al_2O_3$ (Fig. 2 (b)) transducers in solidly mounted, half-released and fully released states. Scans are taken with 2θ swept from 25º to 32.5º (see Supplementary Document, Section 1, Fig. S3 for test-vehicles used for this experiment, and Fig. S4 for wide span XRD scans across 25º to 55º). Both transducers are grown through a similar ALD process and crystallization procedure to enable accurate comparison (See Methods section for detailed growth and crystallization process and Supplementary Document, Section 1, Fig. S2, for visual fabrication process of test-vehicles). Upon mapping diffraction peak

at 30.5º to superimposed orthorhombic (111) / tetragonal (101), superlattice transducers show a single XRD diffraction pattern with consistent orthorhombic phase over the entire release process. On the other hand, monolayer $Hf_{0.5}Zr_{0.5}O_2$ transducers demonstrate a substantial transformation of XRD pattern, with nonpolar diffractions at 28.4º and 31.9º attributed to monoclinic $(\bar{1}11)$ and (111), respectively. The clear suppression of nonpolar monoclinic and preservation of polar orthorhombic phases in superlattice transducers, highlight their superior crystallinity, essential for creation of free-standing piezoelectric NEMS resonators.

Besides sustaining crystallinity and piezoelectricity upon release, $Hf_{0.5}Zr_{0.5}O_2 – Al_2O_3$ superlattice transducers also benefit from a higher mechanical quality factor (Q) compared to pure $Hf_{0.5}Zr_{0.5}O_2$ counterparts. First, the residual tensile stress in superlattice transducers ensure geometrical flatness of released membranes, essential for excitation of lateral bulk acoustic wave (L-BAW) modes[27]. Second, the residual stress in $Hf_{0.5}Zr_{0.5}O_2 – Al_2O_3$ superlattice transducers increases the mechanical energy stored within the resonator and dilutes energy dissipation, resulting in an enhanced Q[39].

To resolve the impact of thickness scaling on $Hf_{0.5}Zr_{0.5}O_2 – Al_2O_3$ superlattice performance, 0.0025 cm^2 solidly mounted (*i.e.*, unreleased) $W/Hf_{0.5}Zr_{0.5}O_2 – Al_2O_3 /W$ capacitors are fabricated with 20nm electrodes and superlattice thickness varied from 10nm (single layer) to 100nm (ten layers). Polarization – electric field hysteresis loops are measured and compared within Supplementary Document, Section 2, Fig. S5. An outward shift in coercive field (E_c) is shown by thicker superlattice capacitors, due to thin Al_2O_3 interlayers acting as a tunneling barrier with a series resistive component[32,40]. This series resistive component ($R_{Al_2O_3}$) also results in slight reduction of transducer k_t^2. However, this effect is negligible in most practical applications, considering the very small value of $R_{Al_2O_3}$[32], compared to the resistance of metal electrodes.

Further, a consistent remanent polarization (P_r) is measured for all thicknesses, confirming ferroelectricity and predominant orthorhombic phase, and highlighting the promise of superlattice thickness scaling with limited performance degradation.

Electromechanical Transduction in $Hf_{0.5}Zr_{0.5}O_2 – Al_2O_3$ Superlattice

The k_t^2 of a piezoelectric transducer is defined as the energy conversion rate between electrical and mechanical domains, and is related to fundamental electrical and electromechanical properties of the film through:

$$k_t^2 = \frac{d_{ki,f}^2 Y}{\varepsilon_0 \varepsilon_i} \tag{1}$$

Here, $d_{ki,f}: i \in (1\ to\ 3), k \in (1\ to\ 6)$ are the thin film, linear piezoelectric coefficients, Y is the Young's modulus of the film, ε_0 is the permittivity of free space, and $\varepsilon_i: i \in (1\ to\ 3)$ is the material's relative permittivity in the direction of applied electric field. k_t^2 sets various performance metrics in NEMS-based frequency control systems. High k_t^2 transducers enable creation of low-impedance resonators for low-power and low-noise oscillators and clocks. Further, the bandwidth and insertion-loss of M/NEMS filters are directly correlated with resonator k_t^2, through linear and inverse relations, respectively.

When using a polycrystalline ferroelectric film for creation of piezoelectric NEMS resonators, the alignment of polar axis in crystalline domains with applied electric field is essential for efficient electromechanical transduction and large k_t^2. Benefiting from switchable polarization direction in ferroelectric domains, application of DC or low-frequency electrical field across thickness direction can be used to ensure a non-zero-sum net polarization in polycrystalline films. Beyond

this behavior, which is known as polling and is common to all ferroelectric transducers, $Hf_xZr_{1-x}O_2$ demonstrates a complex electric-field dependence of electromechanical coupling due to its multi-morph nature and domain-wall motion in its polycrystalline texture.

Experimental literature reports a wide and inconsistent range of positive $d_{33,f}$ coefficients[24,41,42,43] for ferroelectric $Hf_xZr_{1-x}O_2$ films with thicknesses down to 10 nm, and values up to 20 pm•V^{-1}. This upper limit, although impressively large, is a result of linear fitting to an inherently nonlinear displacement-voltage hysteresis loop, which inherently returns an inappropriately linearized piezoelectric value that does not account for quadratic, ferroelastic switching dynamics[36,10,44,45]. Additionally, prior experimental values are at odds with first-principle, density functional theory (DFT) analysis of $Hf_xZr_{1-x}O_2$, which report longitudinal, bulk d_{33} coefficients to be negative[46,47]. These DFT works predict a d_{33} value on the order of -2.5 pm•V^{-1}, meaning that stretching of $Hf_xZr_{1-x}O_2$'s unit cell results in a decrease in polarization[47]. This unusual result, and incongruence with experimental values highlights the need for further study of electromechanical transduction within $Hf_xZr_{1-x}O_2$.

In this work, the ambiguities surrounding electromechanical transduction in ferroelectric $Hf_xZr_{1-x}O_2$ are investigated through accurate monitoring of displacement, current, and polarization hysteresis loops over an extended pulsed poling procedure. Figure 3 shows this pulsed polling evolution, measured in 0.0025 cm^2, W/ $Hf_{0.5}Zr_{0.5}O_2$ – Al_2O_3 /W, solidly mounted (*i.e.*, unreleased)capacitors, with cross section depicted in Fig. 1. For pulsed polling and laser vibrometer measurement specifics, refer to Methods and Supplementary Document Section S4. Figure 3 (a, c ,e) shows displacement (a), polarization (c), and current (e) hysteresis loops across 1 - 50 pulse cycles. Over this quasi-pristine state, the film exhibits antiferroelectric behavior, progressing to relaxed-ferroelectric polarization loops indicative of classical wakeup[36].

Displacement loops show large, nonlinear movement at fields nearing coercive (E_c), becoming less pronounced upon successive pulsed cycling. The combination of pinched/relaxed polarization loops with large quadratic displacement is a characteristic of ferroelastic (non-180º domain) movement[10,45].

In contrast, Fig. 3 (b, d, f) presents displacement (b), polarization (d), and current (f) hysteresis loops across 100 - 1,000 pulse cycles with displacement primarily governed by the linear piezoelectric effect. Here, displacement loops exhibit diminishing, nonlinear movement near +/- E_c, but with a superimposed, linear, butterfly displacement of opposite sign. This inverted butterfly and linear displacement substantiates the negative d_{33} values that is in agreement with *ab initio* works[46,47]. Combining both quadratic (ferroelastic) and linear piezoelectric transduction, assuming zero electric field bias, and considering only small signals, a nonlinear converse piezoelectric effect should be considered:

$$x_i = \sum_{j,k} d_{ki}E_k + f_{ki}E_k + f_{jki}E_jE_k \tag{2}$$

Here, $x_i: i \in (1\ to\ 6)$ is the 6th order strain tensor, $E_k: k \in (1\ to\ 6)$ is the 6th order electric field vector, $d_{ik}: i \in (1\ to\ 3), k \in (1\ to\ 6)$ are linear piezoelectric coefficients, $f_{ik}: i \in (1\ to\ 3), k \in (1\ to\ 6)$ are linear ferroelastic coefficients, and $f_{ijk}: i \in (1\ to\ 3),\ j,\ k \in (1\ to\ 6)$ are quadratic ferroelastic coefficients. Linear ferroelastic coefficients (f_{ik}) are kept separate from linear piezoelectric coefficients (d_{ik}), as they are shown to negligibly contribute to small signal electromechanical transduction (see Supplementary Document, Section 5, for detailed discussions).

Repeated fitting of displacement vs voltage hysteresis loops according to all cycling conditions, yields the evolution of $d_{33,f}$, linear thin film ferroelastic coefficient ($f_{33,f}$), and quadratic thin film

ferroelastic coefficient ($f_{333,f}$) for superlattice $Hf_{0.5}Zr_{0.5}O_2$ – Al_2O_3, displayed in Fig. 4. The presented piezoelectric and ferroelastic coefficients are those directly measured on unreleased superlattice capacitors, without application of any correction factor for conversion to bulk d_{33}[48], as a means of directly addressing inconsistencies of prior reported d_{33} coefficients[24,41,42,43]. Linear coupling coefficients for superlattice $Hf_{0.5}Zr_{0.5}O_2$ – Al_2O_3 progress from unstable large positive, to repeatable, negative values with pulse cycling. Whereas quadratic coupling coefficients progress from unstable large negative to repeatable, near zero values with pulse cycling. To ensure repeatable, linear transduction within superlattice $Hf_{0.5}Zr_{0.5}O_2$ – Al_2O_3, transducers in this work are subject to 1,000 pulse cycles, enabling creation of lateral bulk acoustic wave (L-BAW), and thickness bulk acoustic wave (T-BAW) resonators across SHF and UHF operation. Figure 4 (b, c) depicts displacement vs voltage hysteresis for pristine (1 cycle) and pulse cycled (1k cycle) $Hf_{0.5}Zr_{0.5}O_2$ – Al_2O_3 superlattice transducers, respectively. Dashed lines corresponding to linear and quadratic piezoelectric coefficients fit within the voltage range of 5V to -5V are labeled top left, while insets top right demonstrate how $Hf_{0.5}Zr_{0.5}O_2$'s polar unit cell is dominated by either non-180º domain wall (ferroelastic) movement, or 180º domain wall (piezoelectric) movement.

Superlattice $Hf_{0.5}Zr_{0.5}O_2$ – Al_2O_3 NEMS Resonators

$Hf_{0.5}Zr_{0.5}O_2$ – Al_2O_3 superlattice transducers, sandwiched between top and bottom W electrodes, are used to implement NEMS resonators with frequencies over 0.39 to 17.32 GHz. The resonators are created by patterning interdigitated electrode fingers to enable excitation of lateral- and thickness-oriented bulk acoustic wave modes (*i.e.*, L-BAW and T-BAW modes). The resonator geometries are designed to ensure proper localization of mechanical energy, upon transducer release from the substrate. The fabrication process of these resonators include ALD of $Hf_{0.5}Zr_{0.5}O_2$ – Al_2O_3 superlattice, DC sputtering of W films and their patterning using reactive ion etching

(RIE), DC sputtering of platinum (Pt) routings and pads, RIE of transducer stack to define lateral geometry, and isotropic dry-etching of Si substrate for release. Isotropic release also results in an etch contour that affects resonator performance by extending the acoustic cavity beyond active (*i.e.*, electroded) regions. The extension of energy into the released membrane surrounding resonator active regions may induce additional energy dissipation and corresponding reduction in Q and k_t^2. Despite these negative impacts, a top-side isotropic release method is employed to aid in CMOS compatibility, compared to other methods of release (*i.e.*, back-side). Detailed fabrication process steps are presented in Methods section and visualized in Supplementary Document, Section S6.

L-BAW Resonators

L-BAW resonators operate based on excitation of laterally propagating BAW using interdigitated transducers (IDT). The frequency of L-BAW modes is defined by the IDT pitch size (λ) through:

$$f_{LE} \approx \frac{v_{LE}}{2\lambda} \tag{3}.$$

Here, v_{LE} is the effective velocity of laterally propagating extensional BAW in the transducer. The dependence of L-BAW frequency on λ enables lithographical frequency scaling of resonators implemented in a single batch, simply by changing IDT pitch size and resonator width (*i.e.*, $W = N \cdot \lambda, N \in \mathbb{N}$). This is highly desirable for single-chip integration of multi-frequency and multi-band frequency control systems, critical to the realization of modern multifunctional systems.

In this work, two-port L-BAW resonators with IDT λ spanning over 2µm to 6µm are implemented. Figure 5 (a) shows the SEM image of an L-BAW resonator with 20 IDT fingers, spaced with λ = 2µm, as shown in Fig. 5 (b). Resonator tethers are intentionally kept wide for tensile stress preservation, ensuring a flat structure and enhanced k_t^2. Figure 5(c) illustrates the lateral eigenmode

for a λ = 2µm, L-BAW IDT pair cross section. Two-port spectral characterization of L-BAW resonators are achieved by transmission (S_{21}) responses taken using a Keysight vector network analyzer with measurement specifications provided in Methods section. Scattering parameters are then converted to admittance (Y_{21}) to mitigate port impedance loading of resonator *Q*. Prior to RF characterization, transducers are subject to a pulsed poling procedure, to enhance and stabilize the linear piezoelectricity for resonator operation.

Figure 5 (d) depicts the large-span admittance response magnitude ($|Y_{21}|$) measured for L-BAW resonators with λ = 2µm, 3µm, 4µm, and 6µm. The lithographical frequency scalability of L-BAW mode for different IDT pitch sizes is evident. Besides the fundamental operation mode, each resonator shows various spurious modes corresponding to waves with different polarization (*e.g.*, flexural) or higher-order harmonics of L-BAW. The observed spurious modes may be detrimental to frequency control applications such as reference generation or filtering. However, spurious suppression may be achieved via electrode apodization or dispersion engineering[49, 50, 51]. Figure 5 (e-g) shows $|Y_{21}|$ over a short-span around the L-BAW peaks with lithographically defined frequencies up to 1.374 GHz and series *Q*s exceeding 500. L-BAW k_t^2 values of 1.48%, 1.89%, and 0.84% are extracted for λ = 6µm, 3µm, and 2µm, respectively. Mapping of the fundamental L-BAW mode for each device pitch to Eq. 3 yields a consistent v_{LE} of 5,580 m•s^{-1} for the superlattice transducer. Refer to Supplemental Document Section S7 for measured $|S_{21}|$ responses of resonators within Fig.5, performance metrics of identifiable modes, as well as the f_0, Q and k_t^2 of all measured L-BAW fundamental modes. Although the presented $Hf_{0.5}Zr_{0.5}O_2$ – Al_2O_3 L-BAW resonators allow for lithographical frequency control across UHF (0.3 - 3 GHz), the use of photolithography to pattern IDTs limits the ultimate scalability of $Hf_{0.5}Zr_{0.5}O_2$ – Al_2O_3 L-BAW resonance frequency. Extension to SHF (3 - 30 GHz), either requires the use of high-resolution e-

beam lithography to define sub-1μm IDT pitch or exploiting T-BAW modes with frequencies defined by nanoscale thickness of the superlattice transducer.

T-BAW Resonators

To achieve SHF operation, T-BAW resonators are implemented in $Hf_{0.5}Zr_{0.5}O_2$ – Al_2O_3 superlattice transducers. Figure 6 (a, b) shows the SEM image of a T-BAW resonator, where IDTs are patterned in a waveguide created in $Hf_{0.5}Zr_{0.5}O_2$ – Al_2O_3 superlattice transducers. This architecture enables excitation of high k_t^2-Q resonance modes through acoustic coupling of local T-BAW modes under each IDT finger, across the waveguide. Further, considering the small wavelength of T-BAW, the waveguide dimension in IDT direction (*i.e.*, waveguide aperture) is substantially smaller compared to L-BAW resonators. This ensures suppression of spurious modes that can be excited by BAW propagation orthogonal to the IDT direction.

T-BAW resonators may operate in either extensional or shear modes with frequencies defined by transducer thickness (T) through:

$$f_{TE} \approx \frac{v_{TE}}{2T};\ f_{TS} \approx \frac{v_{TS}}{2T} \tag{4}$$

Here, f_{TE} and f_{TS} are the frequency of extensional and shear modes in T-BAW, while v_{TE} and v_{TS} are effective extensional and shear BAW velocities in the transducer. As evident in Eq. 4, nanoscale thickness of the transducer enables extreme frequency scaling of T-BAW over the SHF spectrum. However, T-BAW resonators lack lithographical frequency scalability available in L-BAW resonators. When operating in thickness-extensional mode, T-BAW resonators benefit from the large longitudinal piezoelectric constant (*i.e.*, $d_{33,f}$) that enables efficient electromechanical transduction with large k_t^2. Shear-extensional modes, on the other hand, can only be excited if the polar axis (*i.e.*, c-axis) of the transducer is misaligned with respect to electric field applied across

thickness[52]. The T-BAW resonators implemented in this work benefit from such rotated c-axis and can be excited in both thickness-extensional and thickness-shear modes. The c-axis rotation is evident in Fig. 1 (d), where the atomic structure shown in the HAADF-STEM image highlights the off axis orientation of polarization direction from surface normal.

T-BAW resonators with IDT pitch sizes of 6μm and 8μm are implemented. Figure 6 (a, b) shows SEM images of T-BAW IDTs in which qualitative mechanical energy localization is achieved via patterning of bottom device W (see Fig. S13 within Supplemental Document, Section 10, for IDT energy profiles). Bottom electrodes are intentionally pattered to include sufficient lithographical tolerance, ensuring complete overlap with top electrode, and uniform electric field across the transducer. Figure 6 (c) illustrates thickness-shear and thickness-extensional BAW mode shapes for an IDT-pair unit cell. The excitation of thickness modes is enabled by applying electric field between top W IDT ports, while keeping bottom electrode floating. Considering one-port operation, the effect of feedthrough due to finite loss tangent within transducer is magnified[53]. This resistive feedthrough loads the performance of resonators and prevents accurate exploration of mechanical resonance and its performance merits. In this work, T-BAW resonators are measured through analytical de-embedding of the resistive feedthrough using electrical test-structures that are implemented in the same batch. In this approach, two non-released structures are used to extract and de-embed the resistive feedthrough between the two transduction ports (See Supplementary Document, Section S8 for detailed de-embedding procedure). Although analytical de-embedding using solidly-mounted structures yields accurate analysis of mechanical resonance, variations in series and shunt impedances resulting from release and top IDT patterning are not captured.

Figure 6 (d) shows the reflectance magnitude ($|S_{11}|$) of T-BAW resonators with 6μm and 8μm pitch size, after resistive feedthrough de-embedding. The two dips observed at 9.42 GHz and 17.32

GHz correspond to the thickness-shear and thickness-extensional BAW modes, respectively. This assumption can be confirmed, considering the frequency insensitivity of these peaks over variation in IDT pitch size. Also considering the 155 nm thickness of the transducer, an effective acoustic velocity of $v_{TE} \approx$ 5,370 ms^{-1} and $v_{TS} \approx$ 2,920 ms^{-1} are extracted for extensional and shear BAW. The similarity of extracted velocities for extensional BAW from both L- and T-BAW resonators ($i.e.$, $v_{LE} \approx v_{TE}$) further confirms the nature of operation modes.

The reflection response is used for extraction of T-BAW admittance around shear and extensional modes. Figure 6 (e, f) shows the admittance ($|Y_{11}|$) for a T-BAW resonator with 6μm pitch size, around the thickness-shear mode at 9.42 GHz and thickness-extensional mode at17.32 GHz. For the thickness-shear resonance mode, a k_t^2 of 0.93% and a series Q of 314.4 are obtained, whereas the thickness-extensional mode a k_t^2 of 2.52% and a series Q of 233.4 are measured.

It should be noted that the large impedance of presented resonators may hinder their adoption in some frequency control applications, such as RF spectral processing, where low insertion loss is essential. For these applications, further improvement of electromechanical coupling and transduction area is required. On the other hand, the impedance of the presented superlattice $Hf_{0.5}Zr_{0.5}O_2$ – Al_2O_3 is low enough to enable creation of integrated oscillators for clock and frequency reference generation. Also, in these applications the envisioned CMOS-BEOL integrability is poised to enable electronic signal conditioning immediately adjacent to acoustic resonators, allowing for considerable performance improvement as well as miniaturization of footprint and power consumption of the system.

Further, the performance merits for T-BAW resonators, despite extreme frequency scaling, demonstrate how superlattice $Hf_{0.5}Zr_{0.5}O_2$ – Al_2O_3 represents a paradigm shift from conventional,

thicker, piezoelectric transducers, thus enabling CMOS monolithic frequency control at super high operational frequencies.

Extraction of L-BAW and T-BAW Resonator Piezoelectric Coefficients

Mapping of parallel and series resonance frequencies within L-BAW and T-BAW admittance responses allows for the accurate extraction of k_t^2. With extracted k_t^2 values, Eq. 1 may be solved considering Y = 308.4 GPa[38] , $\varepsilon_i \approx 35.2$ at 1 GHz[54,55] and $\varepsilon_i \approx 8$ at 17 GHz[54,55] to resolve a loaded, thin film piezoelectric coefficient ($d_{ki,f,l}$) for superlattice $Hf_{0.5}Zr_{0.5}O_2 – Al_2O_3$. Loaded coefficients must be held separate from $d_{ki,f}$ due to the large relative thickness of W electrodes (55nm), and passivation layers (60nm) compared to overall transducer thickness (50nm). Solving Eq.1 for the case of a L-BAW resonator with λ = 3μm and k_t^2 = 1.89%, yields $|d_{31,f,l}|$ = 4.37 pm•V^{-1}. For the case of a T-BAW resonator with λ = 6μm and k_t^2 = 2.52%, evaluation yields $|d_{33,f,l}|$ = 2.41 pm•V^{-1}. Although the thickness-shear mode of T-BAW resonators has a measurable k_t^2 = 0.93%, Eq. 1 cannot be used to evaluate $d_{35,f,l}$ due to superlattice $Hf_{0.5}Zr_{0.5}O_2 – Al_2O_3$ exhibiting an offset polarization axis shown in Fig. 1 (c). With a 2D c-axis projection tilted 15º from applied electric field, the relative effects of $d_{33,f}$ and $d_{35,f}$ cannot be differentiated. Loaded $d_{ki,f,l}$ coefficients may be converted to $d_{ki,f}$ through multiplication of a correction factor (see Supplementary Document, Section S10 for detailed discussion) to compensate for passivation and electrode layer loading and border effects, yielding $d_{31,f}$ = -11.87 pm•V^{-1} and $d_{33,f}$ = -6.46 pm•V^{-1}. The $d_{31,f}$ value extracted from L-BAW resonators is in close agreement with reported coefficients of Si doped HfO_2 = -11.5 pm•V^{-1}, determined via rapid temperature cycling[56]. However, the $d_{33,f}$ value extracted from T-BAW resonators is substantially lower than, and of opposite sign to, the inconsistent range of $d_{33,f}$ up to 20 pm•V^{-1} reported by experimental works[24,41,42,43]. In contrast,

T-BAW extracted coefficients are in good agreement with superlattice $Hf_{0.5}Zr_{0.5}O_2$ – Al_2O_3 $d_{33,f}$ determined via laser vibrometer for clamped capacitors, subject to 1,000 pulse polling cycles. The close match in $d_{33,f}$ coefficients validate the accuracy of both methods, while substantial $d_{31,f}$ and $d_{33,f}$ coefficients highlight the promise of superlattice $Hf_{0.5}Zr_{0.5}O_2$ – Al_2O_3 for the realization of CMOS monolithic frequency control systems.

Resonator Intrinsic Switchability

The ferroelectric nature of superlattice $Hf_{0.5}Zr_{0.5}O_2$ – Al_2O_3 transducers enable intrinsic switchability of NEMS resonators. This is achievable through application of sufficiently large DC electric field to depolarize the transducer and null electromechanical coupling. The intrinsic switchability of NEMS resonators is highly desirable in frequency control applications where reference generation and spectral processing is required over a spread spectrum of multi-frequencies and bands. In these applications, multiplexing an array of resonators, oscillators, and filters with frequencies extending over a wide spectrum requires complex set of external switches that may impose excessive latency, size and power consumption. Intrinsically switchable $Hf_{0.5}Zr_{0.5}O_2$ – Al_2O_3 NEMS resonators obviate the need for external switches and multiplexers, and suppress their overhead on the system.

Here, intrinsic switchability is demonstrated in L-BAW and T-BAW $Hf_{0.5}Zr_{0.5}O_2$ – Al_2O_3 resonators through application of a DC voltage across transducer ports, using a biasTee (see Methods section for detailed measurement setup). Figure 7 (a) depicts measured $|S_{21}|$ responses for a two-port superlattice $Hf_{0.5}Zr_{0.5}O_2$ – Al_2O_3 L-BAW resonator, with positively varied bias, highlighting gradual reduction in resonance peak due to continuous depolarization of the transducer. Upon application of ~8.7 V, the resonator is completely switched off and measurement

only returns the noise floor corresponding to mechanical Brownian noise of the resonator and electronic noise due to the measurement setup. This corresponds to an on/off isolation as large as ~37 dB at room temperature. For repeatability measurements of resonator intrinsic switching, up to 10^6 cycles, refer to Supplemental Document Section S11. To investigate the possibility of intrinsically switching resonators with application of a sufficiently large RF power input, the $|S_{21}|$ response of an L-BAW resonator is measured and reported within Supplemental Document Section S12, with input power level stepped from -15 to 5 dBm.

T-BAW resonators are also subject to intrinsic switching. However, the use of floating bottom electrode and excitation through top IDT ports effectively doubles the switching voltages required for transducer depolarization. Figure 7 (b, c) depicts measured $|Y_{11}|$ responses for the superlattice $Hf_{0.5}Zr_{0.5}O_2$ – Al_2O_3 T-BAW resonator around thickness-shear and thickness-extensional operation modes, for positively varied DC voltage biases. In both modes, gradual reduction of resonance and anti-resonance peaks upon increasing DC bias is evident. When reaching a ~21V, both modes are switched off, leaving the static capacitance of the transducer, resulting in on/off isolation of 7dB and 5dB for shear and extensional modes at 9.42 GHz and 17.32 GHz, respectively.

Conclusions

We have reported the use of superlattice $Hf_{0.5}Zr_{0.5}O_2$ - Al_2O_3 as a CMOS-compatible, nanoscale, intrinsically switchable, piezoelectric transducer, enabling creation of high-*Q* NEMS resonators over 0.39 GHz to 17.32 GHz. The critical role of Al_2O_3 in preserving polar orthorhombic phase within released $Hf_{0.5}Zr_{0.5}O_2$ – Al_2O_3 transducers that is required for NEMS operation was discussed. Further, electromechanical coupling dynamics of superlattice $Hf_{0.5}Zr_{0.5}O_2$ - Al_2O_3 was

investigated via electrical hysteresis measurements and laser vibrometry, revealing a transition from ferroelastic quadratic to linear piezoelectric transduction through pulsed polling. A negative longitudinal piezoelectric coefficient of $d_{33,f}$ = -8.76 pmV^{-1} is measured in linear transduction regime. L-BAW NEMS resonators enabling lithographically scalable, high-Q modes spanning 0.39 to 1.36 GHz are demonstrated as well as T-BAW NEMS resonators with SHF operation up to 17.32 GHz. The extracted *f0*-Q of up to 4.04×10^{12} and k_t^2 of 2.52% at SHF regime and nanoscale thickness, along with perfect CMOS-compatibility of this resonator technology, represent a marked improvement over existing M/NEMS and acoustic counterparts. Additionally, the intrinsic switchability of superlattice $Hf_{0.5}Zr_{0.5}O_2$ – Al_2O_3 resonators is demonstrated, using ferroelectric tailoring of transducer polarization, highlighting an on/off isolation up to 37dB. The presented superlattice $Hf_{0.5}Zr_{0.5}O_2$ - Al_2O_3 NEMS resonators with extreme frequency scalability, high performance and intrinsic switchability show a promising perspective for realization of CMOS-monolithic multi-band frequency control systems in SHF regime.

Methods

ALD of $Hf_{0.5}Zr_{0.5}O_2$ – Al_2O_3 superlattice. Amorphous $Hf_{0.5}Zr_{0.5}O_2$ - Al_2O_3 superlattice transducers are deposited using a Cambridge NanoTech Fiji 200 atomic layer deposition system with a process setpoint of 200 ºC. ~9.2nm thick layers of $Hf_{0.5}Zr_{0.5}O_2$ are deposited using 56 cycles of tetrakis(dimethylamido)hafnium(IV) (TDMAH) and tetrakis(dimethylamido)zirconium(IV) (TDMAZ) precursors pulsed with a 1:1 ratio. 300 W hydrogen and oxygen plasmas are applied following each monolayer deposition for precursor oxidation with enhanced orthorhombic phase concentration[34]. Next, ~1nm thick Al_2O_3 is thermally deposited using 10 cycles of trimethylaluminum (TMA) precursor to limit $Hf_{0.5}Zr_{0.5}O_2$ vertical grain size to <10nm, during further deposition steps. This 9.2nm $Hf_{0.5}Zr_{0.5}O_2$, 1nm Al_2O_3 deposition sub-cycle is then repeated

3 additional times, followed by a final 9.2nm deposition of $Hf_{0.5}Zr_{0.5}O_2$ to form the complete 50nm superlattice.

RTA treatment. Using a SSI Solaris 150, $Hf_{0.5}Zr_{0.5}O_2$ – Al_2O_3 superlattice transducers are annealed for 20s at 500 ºC in nitrogen ambient with un-patterned top and bottom electrodes to promote orthorhombic crystallization. It should be noted that 500 ºC RTA is not essential for crystallization, and could either be replaced by furnace annealing at 325 ºC for 40 min (Supplemental Document Section 3, Fig. S6), or the use of hydrogen plasma to entirely obviate the need for post ALD annealing[34].

TEM characterization. Cross-section samples for TEM imaging are prepared using a FEI Helios Dualbeam Nanolab 600 focused ion beam (FIB) with the final cleaning process using 2 keV Ga ions. Both HR-TEM and HAADF-STEM experiments are carried out using a Themis Z (Thermo Fisher Scientific) operated at the accelerating voltage of 200 keV.

Pulsed polling laser vibrometer measurement. 0.0025 cm^2 W/ $Hf_{0.5}Zr_{0.5}O_2$ – Al_2O_3/ W unreleased, capacitors with cross section depicted in Fig. 1 are measured using a Radiant PiezoMEMS analyzer to obtain polarization and current hysteresis loops depicted within Fig. 3. Testing signals correspond to 15V, bipolar, 1kHz, triangle waves. Pulse cycling signals correspond to 15V, bipolar, 1kHz, square waves. Electrical measurements post 50 cycles are taken with a 2.5V profile bias to better display polarization and current saturation. Displacement measurements are taken using a Polytec NLV-2500 laser vibrometer, connected to a Radiant PizoMEMS analyzer supplying electrical stimulus (see Supplementary Document, Section 4, Fig. S7 for schematic of laser vibrometer measurement). 1 and 10 cycle displacement measurements are single measurements. 20 and 50 cycle displacement measurements are 10 average measurements. 100,

500, and 1k cycle measurements are 100 average measurements. All displacement measurements are taken on a ThorLabs vibration isolation table and postprocessed to remove drift.

NEMS resonator fabrication. Supplementary Fig. S8 summarizes the nine-step fabrication process flow used to realize superlattice $Hf_{0.5}Zr_{0.5}O_2$ – Al_2O_3 L-BAW and T-BAW resonators. Starting with a high resistivity Si wafer, 30nm of $Hf_{0.5}Zr_{0.5}O_2$ passivation layer is deposited via ALD to protect bottom electrodes during release. Next 25nm of W is sputtered and patterned using a sulfur hexafluoride (SF_6) and argon RIE etch to form resonator bottom electrodes, while 150nm of Pt is lifted off for bottom routing. Then, superlattice $Hf_{0.5}Zr_{0.5}O_2$ - Al_2O_3 transducers are deposited by ALD. Top 20nm W is then sputtered and RTA performed. Top device electrodes are pattered using RIE, and top 150nm Pt routing is again lifted off. A symmetric, top 30nm ALD $Hf_{0.5}Zr_{0.5}O_2$ passivation layer is then deposited to again protect the resonant body during release. Access to top and bottom Pt pads are etched using a chlorine (Cl_2), Ar gas chemistry in RIE and thick, 200nm Pt pad plugs are lifted off to form a low resistance resonator contact point. Finally, resonator trenches are defined using a Cl_2 / Ar RIE etch, and the device is released via topside etching of Si using SF_6.

NEMS resonator characterization. Superlattice $Hf_{0.5}Zr_{0.5}O_2$ – Al_2O_3 L-BAW and T-BAW NEMS resonators are measured using a Keysight N5222A vector network analyzer with an input signal power of -15dBm.

Resonator intrinsic switchability. Intrinsic switchability measurements are performed using a Keysight N5222A vector network analyzer with an input signal power of -15dBm capacitively coupled to resonator input port. A benchtop voltage source is also inductively coupled to resonator input port, using a bias-Tee, to apply a variable bias between top and bottom electrodes, tuning transducer polarization.

SEM characterization. SEM images are taken using an FEI Nova NanoSEM 430 system.

DATA AVAILABILITY

The authors declare that the main data supporting the findings of this study are available within the article and its Supplementary Information. Extra data are available from the corresponding author upon request.

Acknowledgement

The authors would like to thank the University of Florida Nanoscale Research Facility cleanroom staff for fabrication support. T.T., F.H. and R.T. acknowledge the financial support from the Defense Advanced Research Projects Agency (DARPA) through the Young Faculty Award (Grant D19AP00044) and National Science Foundation (NSF) through the CAREER award (Grant ECCS-1752206). E.H. and H.K. acknowledge the financial support from the University of Florida through the Research Opportunity Seed Find (ROSF).

References

1. Bereyhi, M. J., Beccari, A., Groth, R., Fedorov, S. A., Arabmoheghi, A., Kippenberg, T. J. & Engelsen, N. J. Hierarchical tensile structures with ultralow mechanical dissipation. *Nat. Commun.* **13,** 1–9 (2022).
2. Kang, J., Matsumoto, Y., Li, X., Jiang, J., Xie, X., Kawamoto, K., Kenmoku, M., Chu, J. H., Liu, W., Mao, J., Ueno, K. & Banerjee, K. On-chip intercalated-graphene inductors for next-generation radio frequency electronics. *Nat. Electron.* **1,** 46–51 (2020).
3. Villanueva, L. G., Karabalin, R. B., Matheny, M. H., Kenig, E., Cross, M. C. & Roukes, M. L. A Nanoscale Parametric Feedback Oscillator. *Nano Lett.* **11,** 5054–5059 (2011).
4. Cha, J. & Daraio, C. Electrical tuning of elastic wave propagation in nanomechanical lattices at MHz frequencies. *Nat. Nanotechnol.* **13,** 6–11 (2018).
5. Chen, C., Lee, S., Deshpande, V. V, Lee, G., Lekas, M., Shepard, K. & Hone, J. Graphene mechanical oscillators with tunable frequency. *Nat. Nanotechnol.* **8,** 923–927 (2013).
6. Ruby, R. A snapshot in time: The future in filters for cell phones. *IEEE Microw. Mag.* **16,** 46–59 (2015).
7. Nguyen, C. T. C. MEMS technology for timing and frequency control. *IEEE Trans. Ultrason. Ferroelectr. Freq. Control* **54,** 251–270 (2007).
8. Pourkamali, S., Ho, G. K. & Ayazi, F. Low-impedance VHF and UHF capacitive silicon bulk acoustic-wave resonators - Part II: Measurement and characterization. *IEEE Trans. Electron Devices* **54,** 2024–2030 (2007).
9. Bhugra, H. & Piazza, G. *Piezoelectric MEMS resonators*. (Springer, 2017).
10. Trolier-Mckinstry, S. & Muralt, P. Thin film piezoelectrics for MEMS. *J. Electroceramics* **12,** 7–17 (2004).
11. Dubois, M. A. & Muralt, P. Properties of aluminum nitride thin films for piezoelectric transducers and microwave filter applications. *Appl. Phys. Lett.* **74,** 3032–3034 (1999).
12. Hopcroft, M. A., Nix, W. D. & Kenny, T. W. What is the Young's Modulus of Silicon ? *J. Microelectromechanical Syst.* **19,** 229–238 (2010).
13. Mahon, S. The 5G Effect on RF Filter Technologies. *IEEE Trans. Semicond. Manuf.* **30,** 494–499 (2017).
14. Nathanson, H. C. & Wickstrom, R. A. A RESONANT-GATE SILICON SURFACE TRANSISTOR WITH HIGH-Q BAND-PASS PROPERTIES. *Appl. Phys. Lett.* **84,** 84–86 (1965).
15. Anderson, J., He, Y., Bahr, B. & Weinstein, D. Integrated acoustic resonators in commercial fin field-effect transistor technology. *Nat. Electron.* **5,** 611–619 (2022).
16. Rawat, U., Bahr, B. & Weinstein, D. Analysis and Modeling of an 11.8 GHz Fin Resonant Body Transistor in a 14 nm FinFET CMOS Process. *IEEE Trans. Ultrason. Ferroelectr.*

Freq. Control **69,** 1399–1412 (2022).

17. Chen, H.-Y., Shih, P.-I., Li, M.-H. & Li, S.-S. 5V-Bias Cmos-Mems Capacitive Resonator with R M < 5KΩ Based On Metal-Insulator-Metal (Mim) Capacitor. in *2022 IEEE 35th Int. Conf. Micro Electro Mech. Syst. Conf.* 1042–1045 (IEEE, 2022). doi:10.1109/MEMS51670.2022.9699766

18. Ledesma, E., Zamora, I., Yanez, J., Uranga, A. & Barniol, N. Single-cell system using monolithic PMUTs-on-CMOS to monitor fluid hydrodynamic properties. *Microsystems Nanoeng.* **8,** (2022).

19. Hudeczek, R., Hager, E., Baumgartner, P. & Pretl, H. Performance Analysis of Resonant-Fin Transistors and Their Application in RF-Circuit Design. *IEEE Access* **10,** 64388–64407 (2022).

20. Tian, D., Chen, P., Yang, X. & Chu, B. Thickness dependence of dielectric and piezoelectric properties from the surface layer effect of BaTiO 3 -based ceramics. *Ceram. Int.* **47,** 17262–17267 (2021).

21. Martin, F., Muralt, P., Dubois, M.-A. & Pezous, A. Thickness dependence of the properties of highly c -axis textured AlN thin films. *J. Vac. Sci. Technol. A* **22,** 361–365 (2004).

22. Nguyen, M. D., Dekkers, M., Vu, H. N. & Rijnders, G. Film-thickness and composition dependence of epitaxial thin-film PZT-based mass-sensors. *Sensors Actuators A. Phys.* **199,** 98–105 (2013).

23. Yandrapalli, S., Liffredo, M., Faizan, M., Kucuk, S., Maillard, D. & Villanueva, L. G. Thin Film Devices for 5G Communications. *Proc. IEEE Int. Conf. Micro Electro Mech. Syst.* **2021-Janua,** 450–453 (2021).

24. Böscke, T. S., Müller, J., Bräuhaus, D., Schröder, U. & Böttger, U. Ferroelectricity in hafnium oxide thin films. *Appl. Phys. Lett.* **99,** (2011).

25. Ghatge, M., Walters, G., Nishida, T. & Tabrizian, R. An ultrathin integrated nanoelectromechanical transducer based on hafnium zirconium oxide. *Nat. Electron.* **2,** 506–512 (2019).

26. Cheema, S. S., Shanker, N., Hsu, C.-H., Datar, A., Bae, J., Kwong, D. & Salahuddin, S. One Nanometer HfO2-Based Ferroelectric Tunnel Junctions on Silicon.pdf. *Adv. Electron. Mater.* **8,** 2100499 (2022).

27. Hakim, F., Ghatge, M. & Tabrizian, R. Excitation of high-frequency in-plane bulk acoustic resonance modes in geometrically engineered hafnium zirconium oxide nano-electro-mechanical membrane. *Appl. Phys. Lett.* **117,** 1–6 (2020).

28. Hakim, F., Tharpe, T. & Tabrizian, R. Ferroelectric-on-Si Super-High-Frequency Fin Bulk Acoustic Resonators with Hf0.5Zr0.5O2 Nanolaminated Transducers. *IEEE Microw. Wirel. Components Lett.* **31,** 701–704 (2021).

29. Shiraishi, T., Katayama, K., Yokouchi, T., Shimizu, T., Oikawa, T., Sakata, O., Uchida, H., Imai, Y., Kiguchi, T., Konno, T. J. & Funakubo, H. Impact of mechanical stress on

ferroelectricity in (Hf0.5Zr0.5)O2 thin films. *Appl. Phys. Lett.* **108,** 0–5 (2016).

30. Park, M. H., Kim, H. J., Kim, Y. J., Lee, W., Moon, T., Kim, K. Do & Hwang, C. S. Study on the degradation mechanism of the ferroelectric properties of thin Hf0.5Zr0.5O2 films on TiN and Ir electrodes. *Appl. Phys. Lett.* **105,** 0–5 (2014).

31. Park, M. H., Lee, Y. H., Kim, H. J., Kim, Y. J., Moon, T., Kim, K. Do, Hyun, S. D., Mikolajick, T., Schroeder, U. & Hwang, C. S. Understanding the formation of the metastable ferroelectric phase in hafnia-zirconia solid solution thin films. *Nanoscale* **10,** 716–725 (2018).

32. Kim, H. J., Park, M. H., Kim, Y. J., Lee, Y. H., Jeon, W., Gwon, T., Moon, T., Kim, K. Do & Hwang, C. S. Grain size engineering for ferroelectric Hf0.5Zr0.5O2 films by an insertion of Al2O3 interlayer. *Appl. Phys. Lett.* **105,** 1–6 (2014).

33. Starschich, S. & Boettger, U. An extensive study of the influence of dopants on the ferroelectric properties of HfO 2. *J. Mater. Chem. C* **5,** 333–338 (2017).

34. Walters, G., Shekhawat, A., Moghaddam, S., Jones, J. L. & Nishida, T. Effect of in situ hydrogen plasma on the ferroelectricity of hafnium zirconium oxide films. *Appl. Phys. Lett.* **116,** (2020).

35. Batra, R., Huan, T. D., Jones, J. L., Rossetti, G. & Ramprasad, R. Factors Favoring Ferroelectricity in Hafnia: A First-Principles Computational Study. *J. Phys. Chem. C* **121,** 4139–4145 (2017).

36. Lederer, M., Olivo, R., Lehninger, D., Abdulazhanov, S., Kämpfe, T., Kirbach, S., Mart, C., Seidel, K. & Eng, L. M. On the Origin of Wake-Up and Antiferroelectric-Like Behavior in Ferroelectric Hafnium Oxide. *Phys. status solidi - Rapid Res. Lett.* **15,** (2021).

37. Riedel, S., Polakowski, P. & Müller, J. A thermally robust and thickness independent ferroelectric phase in laminated hafnium zirconium oxide. *AIP Adv.* **6,** 095123 (2016)

38. Tharpe, T., Zheng, X., Feng, P. X. & Tabrizian, R. Resolving Mechanical Properties and Morphology Evolution of Free-Standing Ferroelectric Hf0.5Zr0.5O2. *Adv. Eng. Mater.* **2101221,** 1–9 (2021).

39. Zheng, X. Q., Tharpe, T., Enamul Hoque Yousuf, S. M., Rudawski, N. G., Feng, P. X. L. & Tabrizian, R. High Quality Factors in Superlattice Ferroelectric Hf0.5Zr0.5O2Nanoelectromechanical Resonators. *ACS Appl. Mater. Interfaces* **14,** 36807–36814 (2022).

40. Jiang, Q., Lee, H. J., Kim, G. H. & Hwang, C. S. The inlaid AI2O3 tunnel switch for ultrathin ferroelectric films. *Adv. Mater.* **21,** 2870–2875 (2009).

41. Kirbach, S., Kühnel, K. & Weinreich, W. Piezoelectric Hafnium Oxide Thin Films for Energy-Harvesting Applications. *Proc. IEEE Conf. Nanotechnol.* **2018-July,** 2018–2021 (2019).

42. Mart, C., Kämpfe, T., Hoffmann, R., Eßlinger, S., Kirbach, S., Kühnel, K., Czernohorsky, M., Eng, L. M. & Weinreich, W. Piezoelectric Response of Polycrystalline Silicon-Doped Hafnium Oxide Thin Films Determined by Rapid Temperature Cycles. *Adv. Electron.*

Mater. **6,** 1–5 (2020).

43. Starschich, S., Schenk, T., Schroeder, U. & Boettger, U. Ferroelectric and piezoelectric properties of Hf1-xZrxO2 and pure ZrO2 films. *Appl. Phys. Lett.* **110,** 2–7 (2017).

44. Xu, F., Trolier-McKinstry, S., Ren, W., Xu, B., Xie, Z. L. & Hemker, K. J. Domain wall motion and its contribution to the dielectric and piezoelectric properties of lead zirconate titanate films. *J. Appl. Phys.* **89,** 1336–1348 (2001).

45. Damjanovic, D. Hysteresis in Piezoelectric and Ferroelectric Materials in *Sci. Hysteresis* (eds. Mayergoyz & Bertotti, G.) **3,** 337–465 (Elsevier, 2005).

46. Liu, J., Liu, S., Yang, J. Y. & Liu, L. Electric Auxetic Effect in Piezoelectrics. *Phys. Rev. Lett.* **125,** 197601 (2020).

47. Dutta, S., Buragohain, P., Glinsek, S., Richter, C., Aramberri, H., Lu, H., Schroeder, U., Defay, E., Gruverman, A. & Íñiguez, J. Piezoelectricity in hafnia. *Nat. Commun.* **12,** 1–10 (2021).

48. Guo, Q; Cao, G. Z.; Shen, I. Y. Measurements of Piezoelectric Coefficient d 33 of Lead Zirconate Titanate Thin Films Using a Mini Force Hammer. *J. Vib. Acoust.* **135,** 1–9 (2013).

49. Giovannini, M., Yazici, S., Kuo, N. K. & Piazza, G. Apodization technique for spurious mode suppression in AlN contour-mode resonators. *Sensors Actuators, A Phys.* **206,** 42–50 (2014).

50. Ghatge, M. & Tabrizian, R. Dispersion-engineered guided-wave resonators in anisotropic single-crystal substrates-Part I: Concept and analytical design. *IEEE Trans. Ultrason. Ferroelectr. Freq. Control* **66,** 1140–1148 (2019).

51. Ghatge, M., Ramezani, M. & Tabrizian, R. Dispersion-Engineered Guided-Wave Resonators in Anisotropic Single-Crystal Substrates - Part II: Numerical and Experimental Characterization. *IEEE Trans. Ultrason. Ferroelectr. Freq. Control* **66,** 1149–1154 (2019).

52. Martin, F., Jan, M.-E., Rey-Mermet, S., Su, D., Muralt, P. & Cantoni, M. Shear mode coupling and tilted grain growth of A1N thin films in BAW resonators. in *IEEE Ultrason. Symp. 2005.* **1,** 333–336 (IEEE, 2005).

53. Dragoman, M., Aldrigo, M., Dragoman, D., Iordanescu, S., Dinescu, A. & Modreanu, M. HfO2-Based Ferroelectrics Applications in Nanoelectronics. *Phys. Status Solidi - Rapid Res. Lett.* **15,** 1–13 (2021).

54. Aldrigo, M., Dragoman, M., Laudadio, E., Iordanescu, S., Modreanu, M., Povey, I. M., Nastase, F., Vulpe, S., Stipa, P., Di Donato, A., Pierantoni, L. & Mencarelli, D. Microwave applications of zirconium-doped hafnium oxide ferroelectrics: From nanoscale calculations up to experimental results. *IEEE MTT-S Int. Microw. Symp. Dig.* **2020-Augus,** 520–523 (2020).

55. Aldrigo, M., Dragoman, M., Iordanescu, S., Nastase, F., Vulpe, S., Dinescu, A. & Vasilache, D. Low-voltage permittivity control of coplanar lines based on hafnium oxide

ferroelectrics grown on silicon. *IEEE Access* **7,** 136686–136693 (2019).

56. Mart, C., Kämpfe, T., Hoffmann, R., Eßlinger, S., Kirbach, S., Kühnel, K., Czernohorsky, M., Eng, L. M. & Weinreich, W. Piezoelectric Response of Polycrystalline Silicon-Doped Hafnium Oxide Thin Films Determined by Rapid Temperature Cycles. *Adv. Electron. Mater.* **6,** 1901015 (2020).

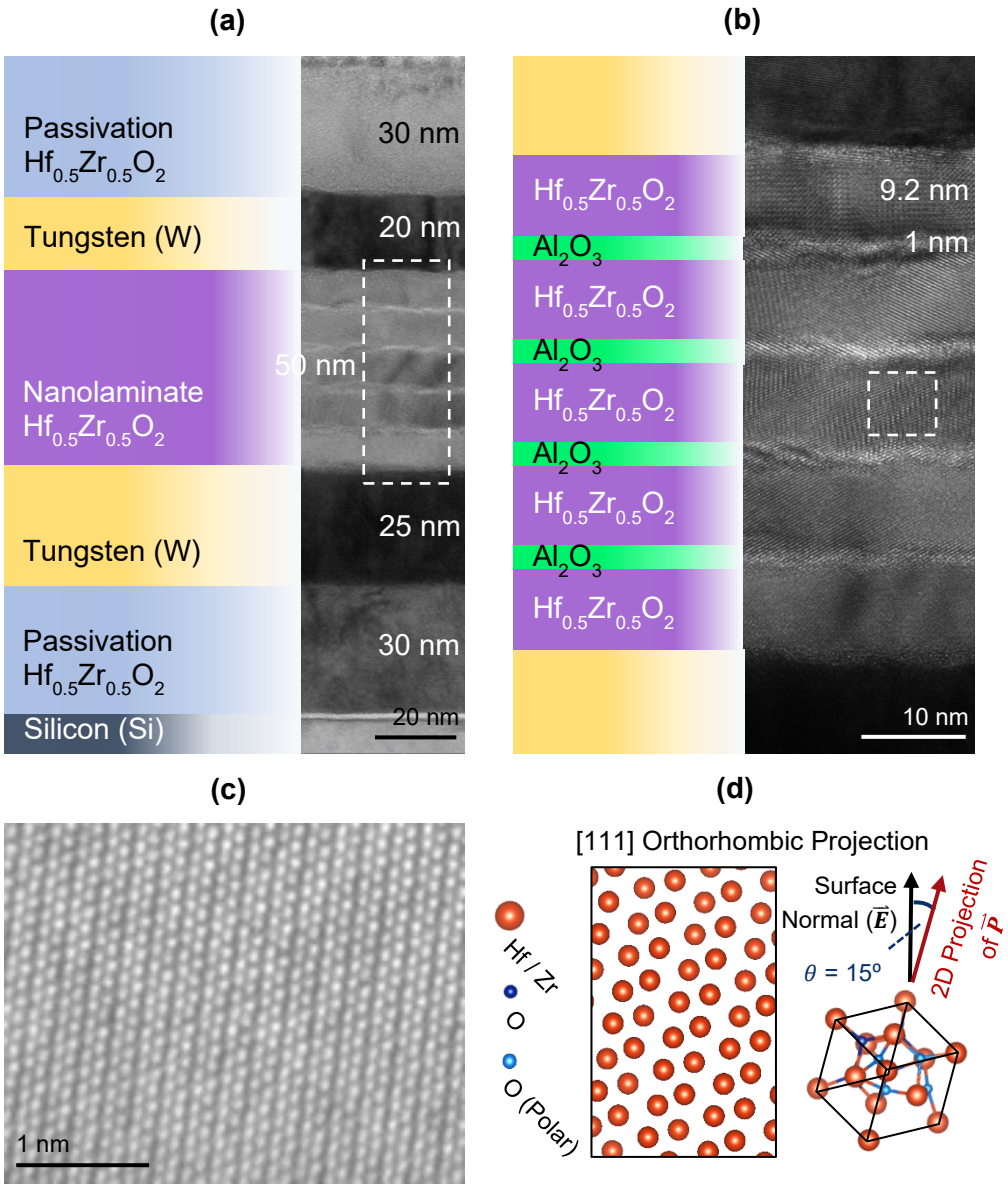

Figure 1. Superlattice $Hf_{0.5}Zr_{0.5}O_2$ – Al_2O_3 Transducer Structure and Morphology. (a) HR-TEM image of the superlattice $Hf_{0.5}Zr_{0.5}O_2$ – Al_2O_3 NEMS resonator with high-level layering annotated. (b) High-magnification HR-TEM image highlighting individual layers in the $Hf_{0.5}Zr_{0.5}O_2$ – Al_2O_3 superlattice transducer, taken from the dashed section in (a) Capping W electrodes supply sufficient tensile stress for the crystallization of $Hf_{0.5}Zr_{0.5}O_2$ following RTA, with multi-morph crystalline phases shown in **Supplementary Fig. S1**. 1nm thermal ALD Al_2O_3 interrupt vertical $Hf_{0.5}Zr_{0.5}O_2$ grain growth and provide a uniform stress gradient across transducer thickness, resulting in a superlattice transducer with reduced monoclinic phase. The depicted $Hf_{0.5}Zr_{0.5}O_2$ layers contain crystallographically separate lattice fringes with varied orientation, characteristic of the superlattice transducer's polycrystalline nature. (c) HAADF-STEM image of the third $Hf_{0.5}Zr_{0.5}O_2$ layer from the dashed box in (b). (d) Atomic mapping of Hf/ Zr atom within

a [111]-projected orthorhombic structure, reconstructed from dashed box in (c). The 2D projection of the polarization direction is shown 15° tilted off the surface normal.

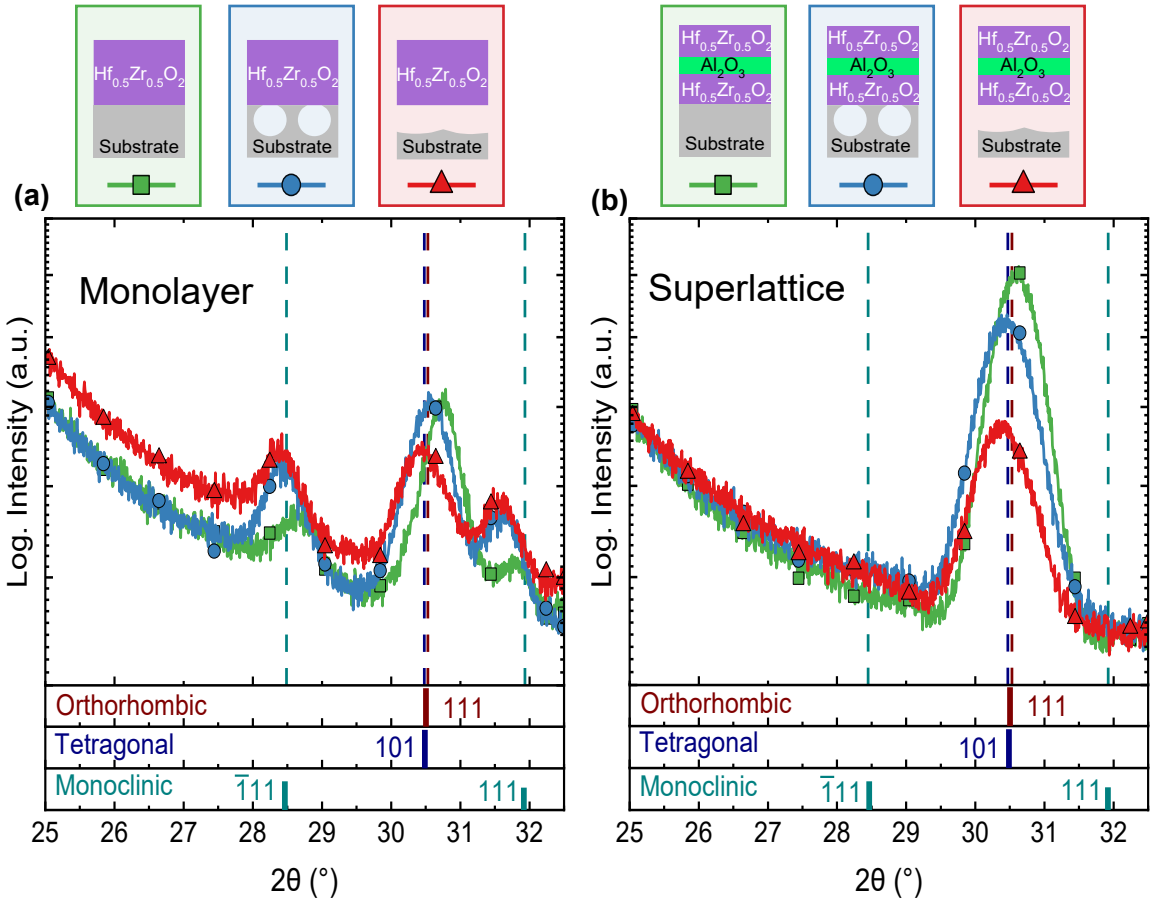

Figure 2. Morphology Evolution of Monolayer $Hf_{0.5}Zr_{0.5}O_2$ and Superlattice $Hf_{0.5}Zr_{0.5}O_2$ – Al_2O_3 Transducer over Release from Substrate. (a) XRD scans with 2θ swept from 25º to 55º for a 20nm thick, electrodeless, $Hf_{0.5}Zr_{0.5}O_2$ monolayer transducer fabricated according to the process depicted in **Supplementary Fig. S2** with growth and crystallization procedures described in Methods. Mapping of experimental diffraction peaks (above) to theoretical peaks (below) resolves the presence of superimposed orthorhombic (111) / tetragonal (101) phases at 30.5º, monoclinic ($\bar{1}11$) phase at 28.4º and monoclinic (111) phase at 31.9º for solidly mounded, half-released, and fully released transducers. (b) XRD scans with 2θ swept from 25º to 55º for a 21nm thick, electrodeless, $Hf_{0.5}Zr_{0.5}O_2$ -Al_2O_3 superlattice transducer with ALD, crystallization, and fabrication processes identical to (a). Mapping of the single experimental diffraction peak resolves the presence of a superimposed orthorhombic (111) / tetragonal (101) phases at 30.5º, consistent across the entire release process. The clear suppression of nonpolar and preservation of polar phases indicates the superior crystallinity of $Hf_{0.5}Zr_{0.5}O_2$ -Al_2O_3 superlattice transducer. Optical images of 20 x 30 mm^2, periodic XRD test structures are presented in **Supplementary Fig. S3**, while extended XRD scans across 25º to 55º 2θ are shown in **Supplementary Fig. S4**.

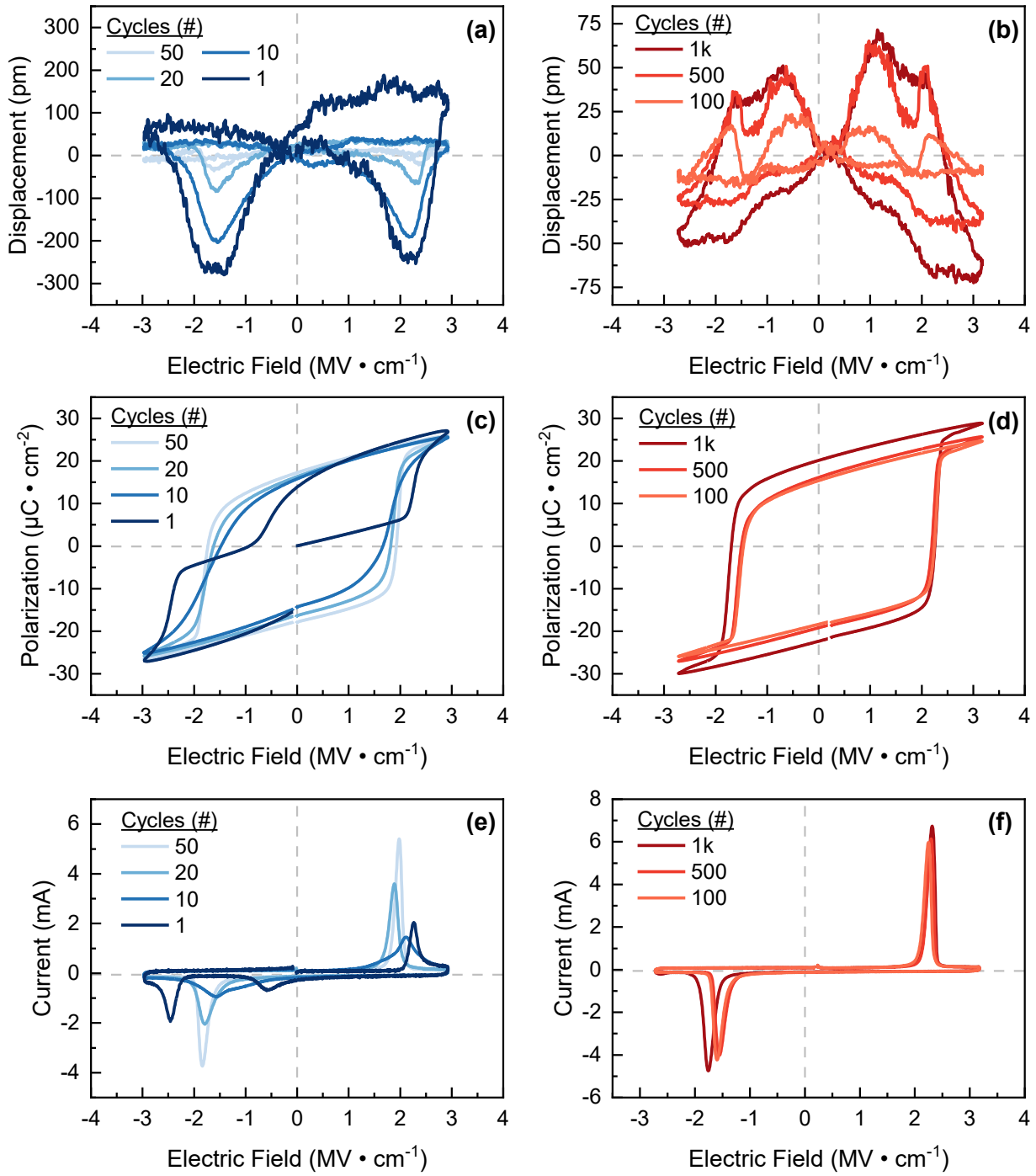

Figure 3. Evolution of Piezoelectric and Ferroelectric Properties in Superlattice $Hf_{0.5}Zr_{0.5}O_2$ – Al_2O_3 Transducers over Pulsed Poling. Displacement, polarization, and current hysteresis loops across pulsed poling based on application of bipolar square pulses with a frequency of 1kHz and voltage of 15V. Pulsed polling hysteresis loops are measured using a 0.0025 cm^2, W/ $Hf_{0.5}Zr_{0.5}O_2$ – Al_2O_3 /W superlattice capacitor, with complete procedure described within Methods. (a, c, e) Quasi-pristine hysteresis loops, up to 50 cycles, for (a) displacement, (c) polarization, and (e) current. Presented pinched/relaxed polarization loops, with large quadratic displacement are characteristic of classical wakeup and ferroelastic (non-180º) domain movement. (b, d, f) Pulsed

polled hysteresis measurements, up to 1,000 cycles, for (b) displacement, (d) polarization, and (f) current. Displacement loops exhibit diminishing, nonlinear movement near +/- E_c, with a superimposed, linear, butterfly displacement of opposite sign, substantiating a negative d_{33} value. Electrical measurements demonstrate pronounced P_r values and gaussian switching currents, characteristic of linear, piezoelectric domain movement.

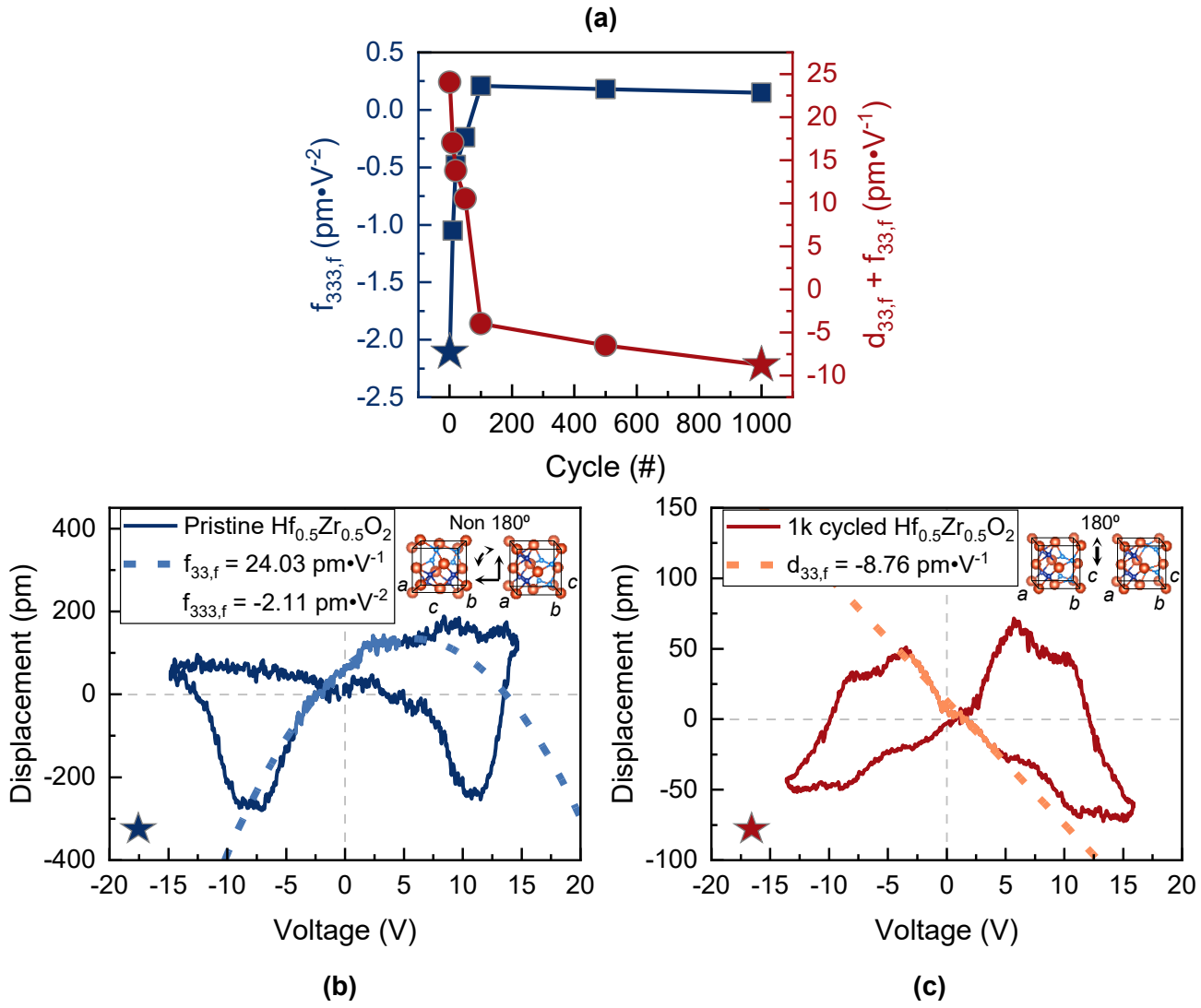

Figure 4. Evolution of Linear and Quadratic Piezoelectric Constants in Superlattice $Hf_{0.5}Zr_{0.5}O_2$ – Al_2O_3 Transducer over Pulsed Poling. (a) Variation of linear thin film piezoelectric coefficients ($d_{33,f} + f_{33,f}$) and quadratic thin film ferroelastic coefficient ($f_{333,f}$) for superlattice $Hf_{0.5}Zr_{0.5}O_2 - Al_2O_3$, subject pulsed polling of 1 to 1,000 cycles (see Methods section for details). (b) Displacement vs voltage for a pristine, single cycle (denoted by blue star) superlattice $Hf_{0.5}Zr_{0.5}O_2 - Al_2O_3$ transducer, with linear and quadratic coefficients extracted from fitting a second-order polynomial around the zero-bias point. (c) Displacement vs voltage for a 1k cycled (denoted by red star) superlattice $Hf_{0.5}Zr_{0.5}O_2 - Al_2O_3$ transducer, with fitted linear coefficient. Insets illustrate dominant crystal structure movement attributed to either ferroelastic (b) or piezoelectric (c) transduction.

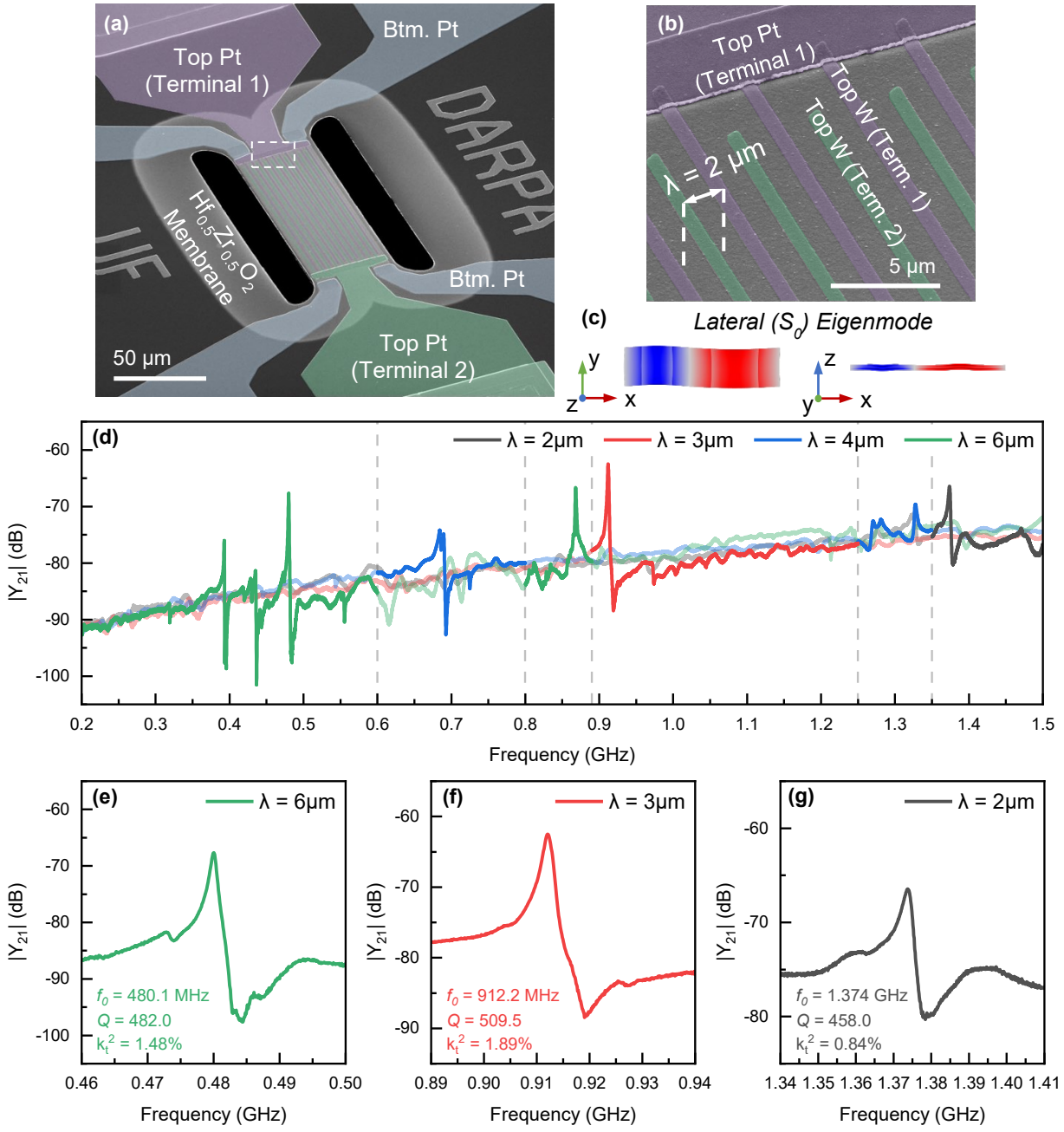

Figure 5. Superlattice $Hf_{0.5}Zr_{0.5}O_2$ – Al_2O_3 L-BAW Resonator Image and Characterization. (a) SEM image of a released, 1,000 cycle pulsed polled, $Hf_{0.5}Zr_{0.5}O_2$ – Al_2O_3 L-BAW resonator with 2μm pitch (λ) and wide tethers for tensile stress preservation. L-BAW resonators are fabricated using a nine-step, CMOS compatible process flow depicted in **Supplementary Fig. S9**. (b) Small scale SEM image of 2μm pitch L-BAW IDTs with highlighted two-port configuration. (c) Top-view and cross-sectional eigenmodes for lateral, S_0 modes excited within L-BAW resonators. (d) Wide span $|Y_{21}|$ responses for L-BAW resonators with varied λ, highlighting precise lithographic frequency control across UHF and consistent velocity of laterally propagating extensional BAW (v_{LE}) of 5,580 m•s^{-1}. (e-g) Small span $|Y_{21}|$ responses corresponding to the

fundamental L-BAW mode for 6µm λ, 3µm λ, and 2µm λ resonators, with annotated resonance frequencies spanning 480.1 MHz to 1.374 GHz, *Q*s exceeding 500 and k_t^2 up to 1.89%. **Supplementary Fig. S10** depicts measured $|S_{21}|$ responses for L-BAW resonators, while **Supplementary Table S1** presents resonator performance metrics for peaks identified.

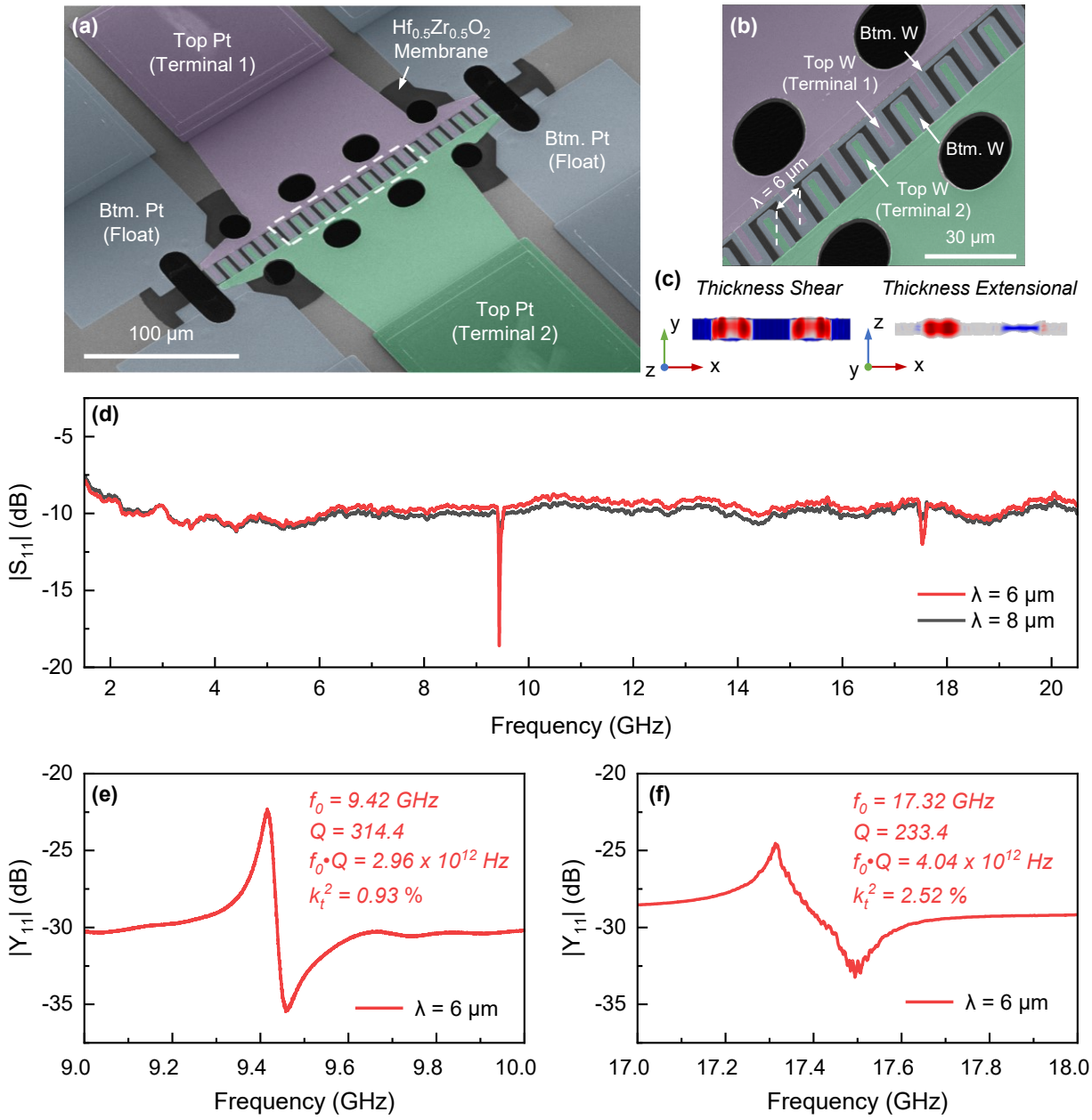

Figure 6. Superlattice $Hf_{0.5}Zr_{0.5}O_2$ – Al_2O_3 T-BAW Resonator Image and Characterization. (a) SEM image of a released, 1,000 cycle pulsed polled, $Hf_{0.5}Zr_{0.5}O_2$ – Al_2O_3 T-BAW resonator with 6μm pitch (λ) and wide tethers for tensile stress preservation. T-BAW resonators are fabricated using a nine-step, CMOS compatible process flow depicted in **Supplementary Fig. S9** (b) Small scale SEM image of 6μm pitch T-BAW IDTs with highlighted one-port configuration. Patterned T-BAW IDTs enable acoustic coupling of local T-BAW modes while the waveguide dimension along IDTs (*i.e.,* waveguide aperture) is minimized for the suppression of spurious modes. (c) Top-view and cross-sectional eigenmodes for thickness shear and thickness extensional modes excited within T-BAW resonators. (d) Wide span $|S_{11}|$ responses following resistive de-embedding (detailed within **Supplementary Section S8**), for T-BAW resonators with varied λ

demonstrating thickness shear BAW excitation at 9.42 GHz and thickness extensional BAW excitation at 17.32 GHz. The depicted pitch-invariant response, along with measured effective shear and extensional BAW velocities in the transducer (v_{TS} and v_{TE}) of 2,920 m•s^{-1} and 5,370 m•s^{-1}, respectively, confirms this assumption of operation modes. (e, f) Small span $|Y_{11}|$ responses corresponding to the thickness shear BAW mode and thickness extensional BAW mode, respectively, for a λ = 6μm T-BAW resonator with $f_0 Q k_t^2$ figure of merit up to 1.02×10^{11} Hz.

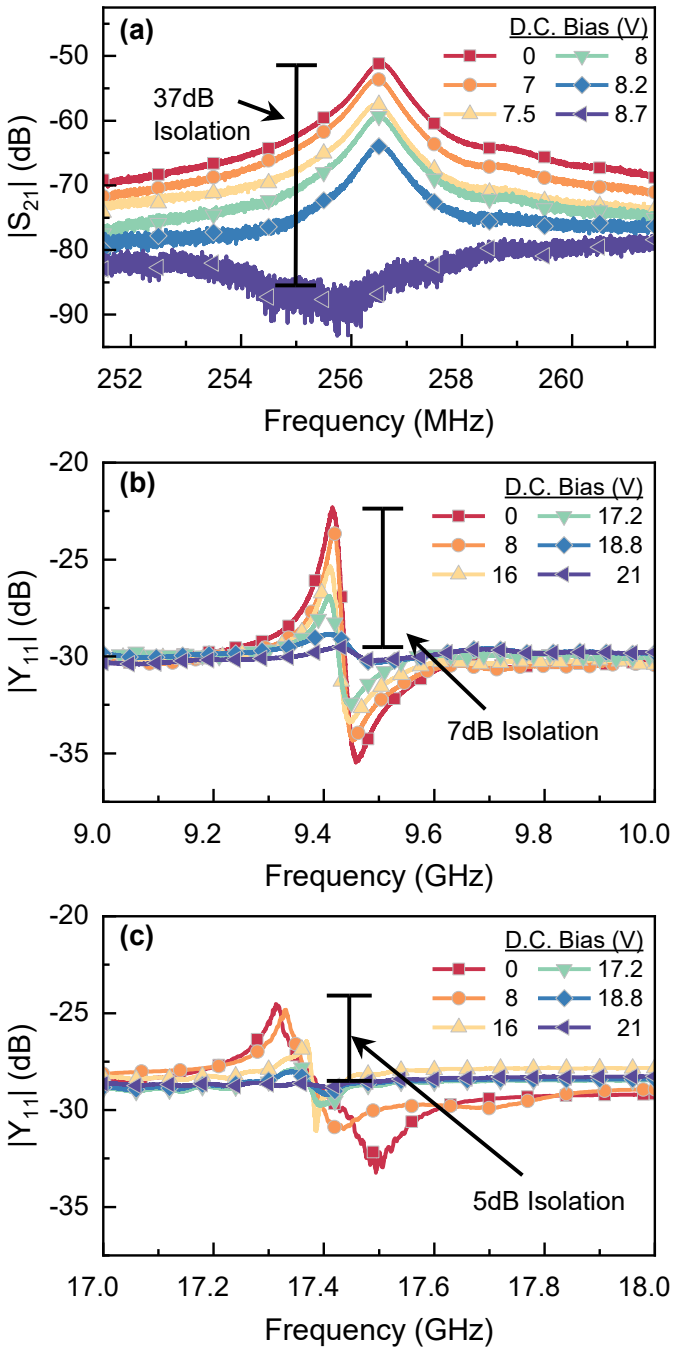

Figure 7. Intrinsic Switchability in Superlattice $Hf_{0.5}Zr_{0.5}O_2$ – Al_2O_3 NEMS Resonators. (a) $|S_{21}|$ response for a two-port, L-BAW resonator with f_0 = 256.5 MHz. Intrinsic switchability with 37dB of on-off isolation is achieved by inductive coupling of 8.7V bias to a capacitively coupled resonator RF input to depolarize the $Hf_{0.5}Zr_{0.5}O_2$ – Al_2O_3 superlattice transducer (biasTee measurement discussed within **Methods**). (b) $|Y_{11}|$ response for thickness shear mode excitation of λ = 6μm T-BAW resonator with f_0 = 9.42 GHz, following resistive de-embedding discussed within **Supplementary Section S8**. Intrinsic switchability with 7dB of on-off isolation upon

application of 21 V via biasTee is achieved due to use of floating bottom electrode and excitation through top IDT ports effectively doubling the switching voltages required. (c) $|Y_{11}|$ response for first order thickness extensional excitation of $\lambda = 6\mu m$ T-BAW resonator with f_0 = 17.32 GHz, following resistive de-embedding, with 5dB of on-off isolation upon application of 21 V bias.